Fully coupled aero-hydrodynamic modelling of floating offshore wind turbines in nonlinear waves using a direct time-domain approach

Deng, Sijia
State Key Laboratory of Coastal and Offshore Engineering, Dalian University of Technology

Liu, Yingyi
Research Institute for Applied Mechanics, Kyushu University

Ning, Dezhi
State Key Laboratory of Coastal and Offshore Engineering, Dalian University of Technology

https://hdl.handle.net/2324/6796349

出版情報：Renewable Energy. 216, pp.119016-, 2023-11. Elsevier
バージョン：
権利関係：

Fully coupled aero-hydrodynamic modelling of floating offshore wind turbines in nonlinear waves using a direct time-domain approach

Sijia Deng[1], *Yingyi Liu*[2], *Dezhi Ning*[1*]

[1]State Key Laboratory of Coastal and Offshore Engineering, Dalian University of Technology, Dalian 116024, China;

[2]Research Institute for Applied Mechanics, Kyushu University, Kasuga 8168580, Japan;

Abstract

In standard operation conditions, a floating offshore wind turbine (FOWT) suffers from the combined action of nonlinear waves and wind. It is essential to explore the effect of higher-order hydrodynamic loads induced by the nonlinear waves on its motion response. In this work, a fully coupled aero-hydrodynamic analysis method for FOWT is developed. The hydrodynamic part is based on the nonlinear potential flow theory and the perturbation approach, using a higher-order boundary element method in the time domain. Blade element momentum theory is applied to evaluate the aerodynamic load on the turbine rotor. The mooring system is modelled by the catenary theory. The developed method is verified against the published data of the NREL's 5-MW baseline wind turbine supported by the DeepCwind semisubmersible platform. The verifications are conducted stepwise in the following ways, including

---

[*] Correspondinb author. (Email: dzning@dlut.edu.cn)

hydrodynamic wave excitation load, free-decay response, the load-displacement relationship of the mooring line, the steady-state response of the wind turbine, and fully coupled aero-hydrodynamic interaction. It is found that the nonlinear effect mainly influences the surge motion. The coupled configuration has little effect on the linear wave force and platform displacement but notably impacts the nonlinear wave force and displacement. The FOWT motion is found to be critical in changing the wave field, the maximum wave elevation position around the platform, and the nonlinear wave force acting on the floating platform. The results illustrate that the traditional indirect time-domain method using the Quadratic Transfer Function (QTF) based on assumed response cannot appropriately evaluate the nonlinear wave force of a FOWT in coupled motions. The results also reveal that nonlinear wave hydrodynamics is necessary to understand the motion response of a fully coupled FOWT.

Keywords: Floating offshore wind turbine; Fully coupled numerical simulation; Higher-order boundary element method

1. Introduction

The world is facing an unprecedented challenge to energy security and the vital goal of achieving carbon neutrality and averting global warming. A permanent fix for the three related problems of energy security, climate change, and affordability is a determined and accelerated effort to transition energy from fossil fuels to renewables. Wind power generation is one of the mature renewable energy technologies that will contribute to the estimated 837 GW of electrical power worldwide in 2022, showing year-over-year growth of 12%, with a total of 94 GW of wind installed around the world in which 21 GW is offshore [1]. Offshore wind turbines are constructed to extract wind power along the coast and in the oceans. Unlike their land-based counterpart, floating wind turbines are located in the deep sea, bringing more challenges to cost management. However, the economic advantage of offshore wind turbines is apparent in terms of more stable year-round wind speed, a higher proportion of high-quality wind energy, greater turbine power, less wind farm development space limitations, and less visual pollution, etc. [2,3].

Offshore wind energy is converted into electricity by wind turbines installed in coastal waters of either bottom-fixed type in shallow sea areas [4] or floating-substructure type anchored to the seabed in deep sea areas [5]. With the continuous development of wind power technology, using only the coastal wind resource cannot meet the needs of industrial and household consumption. About 80% of offshore wind resources are concentrated in waters deeper than 60 m [6], where the installation of conventional bottom-fixed concepts becomes uneconomical, favouring the deployment of floating (buoyant) foundations [5]. Therefore, the future development of offshore wind turbines will be gradually expanded from shallow to deep seas.

However, designing a floating offshore wind turbine (FOWT) system is quite challenging due to the complicated structure, the complex environmental loading, and the coupled effects between the wind turbine, the platform and the mooring system [7]. Numerical simulations are widely adopted in designing a FOWT due to their highly efficient and low-cost merits in contrast to experiments and field tests. A FOWT can be roughly divided into three parts based on the structural and functional features, i.e., turbine, floating platform, mooring system, etc. The motion and the force on each part of a FOWT are interlinked. Firstly, the aerodynamic force on the rotor passes onto the floating support platform via the tower, affecting the dynamic responses of the platform. Secondly, the mooring lines provide restoring forces to the floating platform to restrict its movement. Eventually, the motion of the platform influences the aerodynamic performance of the turbine rotor by changing the relative flow velocity experienced by the rotor blades [8]. Hence, a fully coupled aero-hydrodynamic model is preferable to a reliable numerical prediction of dynamic response in view of the strongly coupled effects.

To date, OpenFAST© is the most commonly used aero-hydro-elastic coupled program for numerical simulations of a wind turbine. It is mainly composed of an aerodynamic module (Aerodyn©), a wind module (InflowWind©), a control module (ServoDyn©), a hydrodynamics module (Hydrodyn©), and other sub-modules [9,10]. The AeroDyn© module is based on the blade element momentum theory (BEM) and the generalised wake model (GDW) to predict aerodynamic loads. HydroDyn© module allows multiple approaches to calculate the hydrodynamic loads on a structure, including the potential-flow theory solution, the strip-theory solution, or a combination of the two [11]. In addition, many investigations on fully-coupled analyses have been conducted using OpenFAST©. Yang et al. [12] developed the F2A© coupled framework to analyse floating offshore wind turbines using FAST© and AQWA™. Roddier [13] integrated FAST© with a hydrodynamic analysis tool named TimeFloat© for fully coupled modelling of WindFloat™. Kvittem et al. [14] incorporated AeroDyn© with the nonlinear FEM software SIMO™/RIFLEX™ to establish a fully coupled model of a 5 MW semisubmersible wind turbine. Shim [15] incorporated FAST© with a hydrodynamic analysis tool CHARM3D to investigate coupled dynamic responses of a 1.5 MW wind turbine supported by a TLP. Karimirad et al. [16] used the SIMO™ [17], REFLEX™ [18], HAWC2™ [19], and FAST© codes to carry out dynamic response analyses.

In addition to OpenFAST©, there exist other commercial software or in-house codes to analyse floating wind turbines. Cunff et al. [20, 21] developed a fully-coupled aero-hydro-servo-elastic simulation tool named DeepLines© for FOWTs. Aerodynamic loads are predicted by the BEMT with the correction of a dynamic stall model, and the blade and tower structures are modelled by the finite element method (FEM). The diffraction and radiation problems of the floating platform are solved by Diodore^{TM}, a commercial hydrodynamic analysis software. Liu et al. [22,23] developed an indirect time-domain method to model the dynamics of a floating truss-structure wind turbine with multiple rotors mounted on the platform's deck. A hybrid panel-stick model is constructed in its hydrodynamic part, incorporating the potential flow theory to evaluate the wave inertia force and a Morison strip method to evaluate the wave drag force. Chen et al. [24] developed an aero-hydro-servo-elastic coupled tool (DARwind©) based on Kane's kinetic equation and BEMT. The hydrodynamic load is evaluated by the second-order frequency domain potential flow theory. The DARwind© tool is validated extensively against experimental results. Frank [25] developed a model named SLOW© using an iterative response calculation with a reduced-order frequency-domain method. It has heave plate drag coefficients, which are parameterised functions of literature data. In addition to these tools, Bladed^{TM} and HAWC2^{TM} are well-known commercial software for designing wind turbines. Both employ BEMT to evaluate aerodynamic loads and the multi-body dynamic (MBD) method for structural modelling, having high efficiency in examining aero-elastic effects [26-29]. In the aforementioned tools, the hydrodynamic analysis usually applies the indirect time-domain method, using Fourier's transform to convert hydrodynamic force coefficients pre-calculated in the frequency domain to the time domain. For a moving body, the quadratic transfer function (QTF) can be induced by not only the waves but also the first-order motion response. Based on the Cummins method, the second-order excitation force in the time domain is conventionally evaluated by the Fourier transform of the QTF. This will request that QTF be calculated according to the transient motion response at each time step to solve the motion response at the next time step, and so on. Since the computation burden in such a manner is almost unbearable, the common way that people are doing instead is to use a fixed-body QTF throughout all time steps so that the QTF needs to be calculated only once. It will lead to inaccuracy of the time-domain simulation. In contrast, a direct time domain is free of such a problem as there is no need to calculate the QTF.

On the other hand, in the drive for greater accuracy of floating wind energy, high-fidelity models play an essential role in developing FOWTs. Tran [33] has performed a series of unsteady aerodynamic simulations for turbine blades by considering the platform motion with periodical surge, pitch, or yaw with a dynamic moving grid technique. Besides the oscillating regularity of thrust and power, the flow interaction phenomena between the turbine blades with oscillating motions and the generated blade-tip vortices are found. Wu [34] developed a CFD model for unsteady and nonlinear aerodynamic simulations of a rotor under floating platform-induced motions with an arbitrary mesh interface (AMI). Liu [35] established a fully coupled CFD analysis tool for FOWTs based on the open-source CFD package OpenFOAM© and studied the dynamics of the OC4 DeepCWind semisubmersible FOWT. CFD simulations achieve accurate results and enable detailed quantitative flow field analysis. Cheng [8] developed the FOWT-UALM-SJTU© solver based on OpenFOAM©, incorporating an unsteady actuator line model (UALM) to simulate the aerodynamics of a wind turbine and a two-phase CFD solver naoe-FOAM-SJTU© to solve the hydrodynamics of the floating platform. In the coupled model, the three-dimensional Reynolds-Averaged Navier-Stokes (RANS) equations are solved with the turbulence model k-ω SST, and the Pressure-Implicit with Splitting of Operations (PISO) algorithm is applied to solve the pressure-velocity coupled equations. In general, CFD methods have great accuracy but huge simulation cost, which is inappropriate for dealing with many engineering cases.

Existing hydrodynamic methodologies applied to FOWTs mainly consist of CFD and potential-flow-based methods. Potential-flow-based methods have several variants. A direct time-domain method does not need to have problematic QTF values as the input because the hydrodynamic forces are directly calculated at each time step. For this reason, a time-domain method is more suitable for predicting the response of the floating system. In view of this point, a direct nonlinear time-domain method is preferable to act as the base for the aero-hydrodynamic coupled in modelling a FOWT.

The primary purpose of the present study is to develop a new aero-hydrodynamic coupled methodology that directly considers nonlinear waves in the time domain. The theory and numerical methods are introduced in Section 2. Validations of the sub-modules and the fully coupled model are given in Section 3 against experimental results and the published data. Moreover, a numerical simulation of the 5 MW DeepCwind semisubmersible FOWT is presented, demonstrating the model's superiority in capturing the platform's nonlinear effects. The coupled effect of FOWT considering nonlinear hydrodynamic load is investigated and discussed in Section 4. Conclusions are drawn in Section 5 based on the previous analysis.

2. Mathematical formulation and numerical methodology

2.1 Hydrodynamic method

Based on the nonlinear potential flow theory, a second-order 3D time-domain HOBEM is applied to investigate the hydrodynamic performance of a FOWT system. Fig. 1 defines the global and the local coordinate systems in the computation. The first is space-fixed, denoted as $Oxyz$, the origin of which is located on the still water surface, while the other is body-fixed, denoted as $O'x'y'z'$ (fixed on the platform mass centre). At the initial static equilibrium position, the two systems coincide.

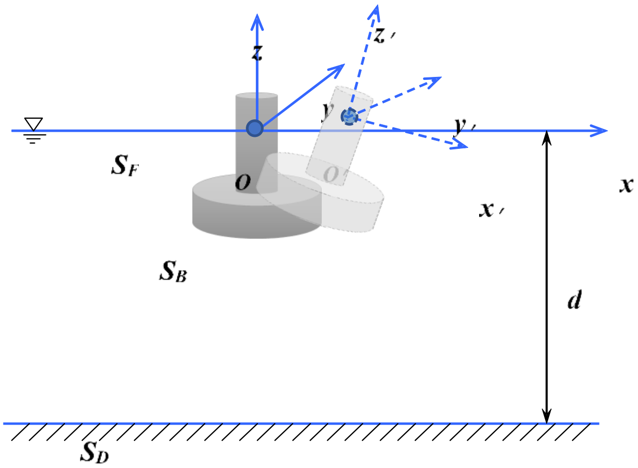

Fig.1. Definition sketch of coordinate systems and the computation domain

The fluid is assumed incompressible and inviscid. The wave field around the floating foundation can be described by a complex spatial potential $\varphi(x, y, z, t)$, which satisfies the Laplace equation. The spatial potential φ can be divided as a known incident potential φ_i and an unknown scattered potential φ_s [36]. Following the perturbation expansion technique up to the second order, the scattered potential satisfies the Laplace equation:

$$\nabla^2 {\varphi_s}^{(m)}(x, y, z, t) = 0, \tag{1}$$

where the superscript *m* (1 or 2) denotes the order of the perturbation expansion. The impermeability conditions at the bottom S_D and the solid body surface S_B read

$$\frac{\partial \phi_s^{(m)}}{\partial n} = -\frac{\partial \phi_i^{(m)}}{\partial n}, \text{on } S_D \text{ and } S_B \tag{2}$$

where $\frac{\partial}{\partial n}$ denotes the normal derivative on the solid surface. To analyse the wave motion in a finite domain, a sponge layer is introduced to absorb the reflected waves from the platform [37]. Using Taylor's expansion, the kinematic and dynamic boundary conditions on the free surface S_F can be expressed as

$$\frac{\partial {\eta_s}^{(m)}}{\partial t} = \frac{{\varphi_s}^{(m)}}{\partial z} - \nu_{(r)} {\eta_s}^{(m)} - f_m' \ (m = 1 \text{ or } 2), \tag{3}$$

$$\frac{\partial \phi_s^{(m)}}{\partial t} + g\eta_s^{(m)} + \nu_{(r)}\phi_s^{(m)} - f_m'' = \begin{cases} \dfrac{\partial \phi^{(1)}}{\partial n} & (m = 1) \\ -\left(\eta^{(1)} \dfrac{\partial \phi^{(1)}}{\partial n} + \dfrac{\partial \phi^{(2)}}{\partial n}\right) & (m = 2) \end{cases}, \tag{4}$$

where η_s denotes the scattered wave elevation around the platform, $\nu_{(r)}$ is the damping coefficient of the sponge layer. The damping coefficient $\nu_{(r)}$ is expressed by

$$v(r) = \begin{cases} \alpha_0 \omega \left(\dfrac{r - r_0}{\beta_0 \lambda}\right)^2 & r_0 \leq r \leq r_\mathrm{i} = r_0 + \beta_0 \lambda \\ 0 & r < r_0 \end{cases}. \tag{5}$$

Green's second identity is applied to the boundary value problem, i.e., Eq. (1) ~ (4), by using the Rankine source and its image with respect to the seabed as the Green function [36]

$$G\left(p_s, q_f\right) = -\frac{1}{4\pi}\left(\frac{1}{R_0} + \frac{1}{R_z}\right), \tag{6}$$

where $p_s = (x_1, y_1, z_1)$ and $q_f = (x, y, z)$ are the source and the field point, respectively, and

$$R_0 = \sqrt{(x - x_1)^2 + (y - y_1)^2 + (z - z_1)^2}, \tag{7}$$

$$R_z = \sqrt{(x - x_1)^2 + (y - y_1)^2 + (z + z_1 + 2h)^2}, \tag{8}$$

As such, an integral equation for the scattered wave potential can be obtained as

$$\alpha\varphi_s(p_s) = \iint_S \left[\varphi_s\left(q_f\right)\frac{\partial G(q_f, p_s)}{\partial n} - G\left(q_f, p_s\right)\frac{\partial \varphi_s(q_f)}{\partial n}\right] dS, \tag{9}$$

where the boundary surface S includes the mean free surface (S_F) and the solid surface (S_D), and α is the solid angle coefficient. The boundary integral equation, Eq. (9), is discretised by a higher-order boundary element method and solved by the fourth-order Adams-Bashforth predictor-corrector method. The readers are referred to Jin et al. [39] for the detailed procedure.

Wave force and moment on the platform are then evaluated by integrating the dynamic pressure over the wet surface of the platform:

$$F = \iint_{S_{\text{platform}}} pn dS, \tag{10}$$

$$M = \iint_{S_{\text{platform}}} p[(z - z_0)n_x - (x - x_0)n_z] dS, \tag{11}$$

where $n = \left(n_x, n_y, n_z\right)$, and $F = \left(F_x, F_y, F_z\right)$. (x_0, y_0, z_0) is the rotational centre defined to be the platform mass centre. The subscript "platform" denotes the wet surface of the floating foundation.

2.2 *Aerodynamic method*

The BEMT assumes that the blades can be divided into small annular elements operating aerodynamically as two-dimensional airfoils [40] to conduct aerodynamics calculation of the rotor, as shown in Fig. 2. Given the lift and drag coefficients of all the airfoils, the lift and drag forces acting on the blade at spanwise location *r* are evaluated by

$$L = \frac{1}{2}\rho_a V_{rel}^2 c C_l, \tag{12}$$

$$D = \frac{1}{2}\rho_a V_{rel}^2 c C_d, \tag{13}$$

where ρ_a is the air density, c the chord length of the blade element, L and D respectively the lift and the drag force of the sectional airfoil, C_l and C_d respectively the lift and the drag coefficients, V_{rel} the absolute wind speed.

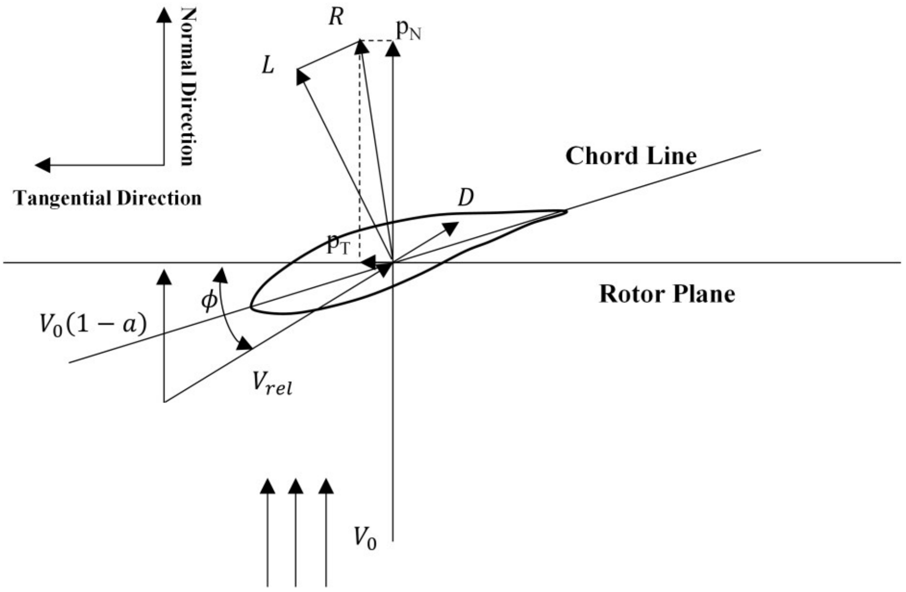

Fig. 2. Illustration of wind velocities and local loads at the spanwise location *r*

By expressing the lift and the drag force in the axial and the tangential directions through a coordinate transformation, it is known that

$$p_N = L\cos\,\phi + D\sin\,\phi, \tag{14}$$

$$p_T = L\sin\,\phi - D\cos\,\phi, \tag{15}$$

$$\tan\,\phi = \frac{(1-a)V_0}{(1+a')\omega r}, \tag{16}$$

where ϕ is the wind inflow angle, a the axial induction factor, $a'$the tangential induction factor, ω the rotor rotational speed, and r the local radius of the blade element.

The axial thrust force F_T and the torque M_T can be derived from the two-dimensional blade element theory:

$$F_T = \int_r Bp_T dr = \int_r \frac{1}{2}\rho_a B V_{rel}^2 c(C_l \sin\phi - C_d \cos\phi)\mathrm{d}r, \tag{17}$$

$$M_T = \int_r rBp_T dr = \int_r \frac{1}{2}\rho_a B V_{rel}^2 c(C_l \sin\phi - C_d \cos\phi) r\mathrm{d}r, \tag{18}$$

where B is the number of blades. By resolving the distribution of the normal and the tangential loads along the span of blades, the total thrust force and the aerodynamic torque are obtained based on the linear variation assumption of the load distribution between neighbouring blade elements [41]. In addition, to consider the influence of vortex shedding from the blade tips into the wake on the induced velocity field [40], the most widely acknowledged Prandtl's model for tip-loss correction [42] is adopted in this study.

Aerodynamic force at the tower is simplified as a lumped force and moment that act at the centre of the resulting wind load of the platform. The lumped force is denoted as follows:

$$F_H = \frac{1}{2}\pi \rho_a C_D A U_{\mathrm{rel}(z^*)}^2, \tag{19}$$

where C_D is the drag coefficient on the tower; $U_{\mathrm{rel}(z^*)}$ is the relative velocity between the wind and the tower measured at the elevation z^*; A is the tower's projected area above the mean water level. Force on the tower could be represented in Eq. (3) as follows:

$$F_H = \int_{z=bottom}^{z=top} \mathrm{d}F(z)\mathrm{d}z = \frac{1}{2}\pi\rho_a C_D \int_{z=bottom}^{z=top} D(z) U_{\mathrm{rel}}^2(z)\mathrm{d}z. \tag{20}$$

2.3 Baseline control system

The NREL 5-MW baseline wind turbine is set in a conventional variable-speed, variable blade-pitch configuration. In such wind turbines, the traditional approach for controlling power-production operation relies on the design of two basic control systems: a generator-torque controller and a full-span rotor-collective blade-pitch controller.

Under low wind speed conditions, variable-speed wind turbines operate at maximum efficiency around the optimum tip speed ratio with a fixed pitch angle. The generator torque is simulated as a function of the generator speed.

Under high wind speed conditions, variable blade-pitch configuration [43] takes over. Because the goal of the blade-pitch control system is to regulate the generator speed, the single DoF of the angular rotation of the shaft is used. To compute the required control gains, the simple free-body diagram of the drivetrain $\Delta\theta$ follows the equation:

$$\Delta\theta = K_P N_{\text{Gear}}\,\Delta\Omega + K_I \int_0^t N_{\text{Gear}}\,\Delta\Omega dt + K_D N_{\text{Gear}}\,\Delta\dot{\Omega}, \tag{21}$$

where K_P, K_I, and K_D are the blade-pitch controller proportional, integral, and derivative gains, respectively; N_{Gear} is the high-speed to low-speed gearbox ratio; $\Delta\Omega$ is the small perturbation of low-speed shaft rotational speed about the rated speed; $\Delta\dot{\Omega}$ is the first-time derivative of $\Delta\Omega$.

2.4 Mooring system

A mooring chain consists of fairlead, line, and anchor. The following basic assumptions are pre-defined in the construction of the mooring system model: (1) the horizontal, rigid, and frictionless seabed surface, (2) the prolonged movement of each part of the anchor chain in the water, (3) the ignored inertia force of the anchor chain, (4) the elongation caused by the initial tension initial length of the mooring line and chain line, and (5) the unmoveable anchor point.

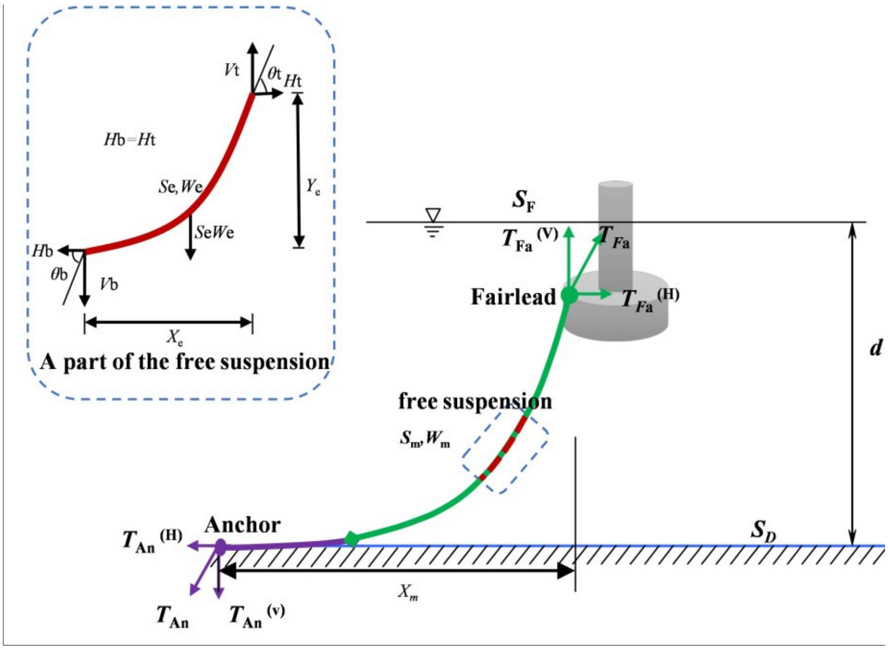

Fig. 3. Schematic diagram of the dynamic model of a mooring line

Since the relationship between force and displacement is nonlinear, the anchor chain force must be solved by an iterative method. The catenary equation [44] is used to find the relationship between the anchor chain force and the displacement. For any freely suspended part, the horizontal projection and vertical projection, as shown in Fig. 3, can be expressed as

$$Y_e = \left(\frac{H_t}{W_e}\right)\left(\cosh\left(\frac{1}{\sinh(\tan\theta_t)}\right)\right) - \cosh\left(\frac{1}{\sinh(\tan\theta_b)}\right)\Big), \tag{21}$$

$$X_e = \left(\frac{H_t}{W_e}\right)\left(\frac{H_t}{W\sinh\,(\tan\theta_t)} - \frac{1}{\sinh\,(\tan\theta_b)}\right), \tag{23}$$

$$\tan\theta_b = \frac{V_t - W_e S_e}{H_t}, \tag{24}$$

$$V_t = H_t \tan\ \theta_t. \tag{25}$$

where X_e and Y_e are the horizontal and the vertical component of element length; θ_t is the angle between the end of the element and the horizontal plane; θ_b is the angle between the beginning of the element and the horizontal plane; V_b and V_t are the horizontal and the vertical component of the element tension; H_b and H_t are the horizontal and the vertical component of the element end tension; W_e is the weight of the element; S_e is the element length. If H_t, θ_t, and W_e are known, then

$$\tan\theta_b = \sinh\left(\frac{1}{\cosh\left(\cosh\left(\frac{1}{\sinh(\tan\theta_t)}\right) - \left(\frac{Y_e W_e}{H_t}\right)\right)}\right), \tag{26}$$

$$S_e = \frac{H_t(\tan\theta_t - \tan\theta_b)}{W_e}. \tag{27}$$

The horizontal projection X of the anchor chain can be calculated by Eq. (23). For a specific section, it is supposed that the initial tension of the section is T_0 and the corresponding initial length is S_0. When the tension is T, the length of the element can be expressed as

$$S_\mathrm{e} = S_0\left(1 + \frac{(T - T_0)}{EA}\right), \tag{28}$$

where E and A are Young's Modulus and effective area, respectively. The total weight of the chain remains unchanged, and the weight per unit length in water can be calculated as:

$$W_{\mathrm{e}} = \frac{S_0 W_0}{S_{\mathrm{e}}}, \tag{29}$$

where W_0 is the initial weight per unit length of the anchor chain in water. W_m is the weight of the free suspension of the mooing line. S_e is the length of the free suspension of the mooing line. T_{Fa} is the fairlead tension. ${T_{\mathrm{Fa}}}^{(\mathrm{v})}$ and ${T_{\mathrm{Fa}}}^{(\mathrm{H})}$ are the horizontal and the vertical component of T_{Fa} . T_{An} is the anchor tension. ${T_{\mathrm{An}}}^{(\mathrm{v})}$ and ${T_{\mathrm{An}}}^{(\mathrm{H})}$ are the horizontal and the vertical component of T_{An}. The horizontal distance between the fairlead and the anchor is referred to as X_{m}. S_m is the distance along the line from the fairlead to the equivalent point on the unstretched mooring line where the point on the stretched mooring line first touches the seabed.

2.5 Coupled framework

In order to conduct the fully coupled simulation, the three parts consisting of the hydrodynamic module, the mooring module, and the aerodynamic module, are combined logically to develop a coupled framework presented in Fig. 4.

The position and velocity of the platform calculated in the hydrodynamic module are used to determine the motion response of the wind turbine. The aerodynamic load at the tower basement and the lumped force acting on the tower calculated by the aerodynamic module are added to the right-hand side of the motion equation as external forces. The motion equation of the platform includes a linear equation and a nonlinear equation:

$$[M]\ddot{\xi}^{(1)} + [B]{\dot{\xi}^{(1)}}^2 + [C]\xi^{(1)} = F_D^{(1)} + F_M^{(1)} + F_T^{(1)} + F_H^{(1)}, \tag{30}$$

$$\begin{aligned} &[M]\ddot{\xi}^{(2)} + [B]{\dot{\xi}^{(2)}}^2 + [C]\xi^{(2)} = F_D^{(2)} + F_I^{(2)} + F_Q^{(2)} + F_W^{(2)} + F_M^{(2)} \\ &+F_T^{(2)} + F_H^{(1)} + \begin{Bmatrix} 0 \\ \mathrm{m}_r^{(2)} \end{Bmatrix} \end{aligned}, \tag{31}$$

$$\xi^{\mathrm{total}} = \xi^{(1)} + \xi^{(2)}, \tag{32}$$

$$F^{\mathrm{total}} = F_D^{(1)} + F_D^{(2)} + F_I^{(2)} + F_Q^{(2)} + F_W^{(2)}, \tag{33}$$

where $\xi^{(1)}$ and $\xi^{(2)}$ are the first-order and the second-order displacements. $[M]$, $[B]$ and

$[C]$ denote the rigid body mass matrix, viscous damping matrix, and restoring force matrix, respectively. $F_D^{(1)}$ is the first-order hydrodynamic force. $F_M^{(1)}$ is the mooring load induced by the first-order platform displacement. $F_T^{(1)}$ and $F_H^{(1)}$ are the aerodynamic force on the rotor and the tower when the platform responds to the first-order displacement, respectively. $F_D^{(2)}$ is the second-order hydrodynamic force. $F_I^{(2)}$ is the contribution from the second-order potential. The sum of $F_Q^{(2)}$ is the second-order force contribution term of the object movement. $F_M^{(2)}$ is the mooring tension induced by the second-order platform displacement, and $F_T^{(2)}$ and $F_H^{(2)}$ are the aerodynamic force on the rotor and the tower when the platform responds to the second-order displacement. $\begin{Bmatrix} 0 \\ \mathrm{m}_r^{(2)} \end{Bmatrix}$ is generated by the interaction between the first rotational displacements [31]. The total displacement $\xi^{(\mathrm{total})}$ is the sum of $\xi^{(1)}$ and $\xi^{(2)}$ as Eq. (32). All the variables in Eq. (31) to (33) are vectors.The total hydrodynamic load is $F^{(\mathrm{total})}$. The subscript of F and ξ represents the direction of the surge ($_1$), sway ($_2$), heave ($_3$), roll ($_4$), pitch ($_5$), and yaw ($_6$) in the following figures.

Eqs. (30) and (31) illustrate that the solutions of all the forces and the motion are coupled with each other. The aerodynamic module is used to obtain the load on the tower according to the response of the platform at the current time t_n by overlapping the coordinates of the tower. The tension of the mooring system can be obtained from the mooring module according to the platform response at the current time t_n by matching boundary conditions at fairleads. It is noted that there are two kinds of platform responses, the linear motion response and the non-linear response. The linear response is calculated considering only the first wave force. The nonlinear response is calculated by considering the second wave force as well. The aerodynamic load and the mooring load can be calculated knowing the nonlinear platform displacement. The results are transformed into forces acting on the centre of mass of the platform by appropriately changing the unified coordinate system. Eqs. (21) and (22) are used to predict the next time step ($t_{n+1} = t_n + \Delta t$) of the platform response. These processes present are repeated until the simulation ends successfully.

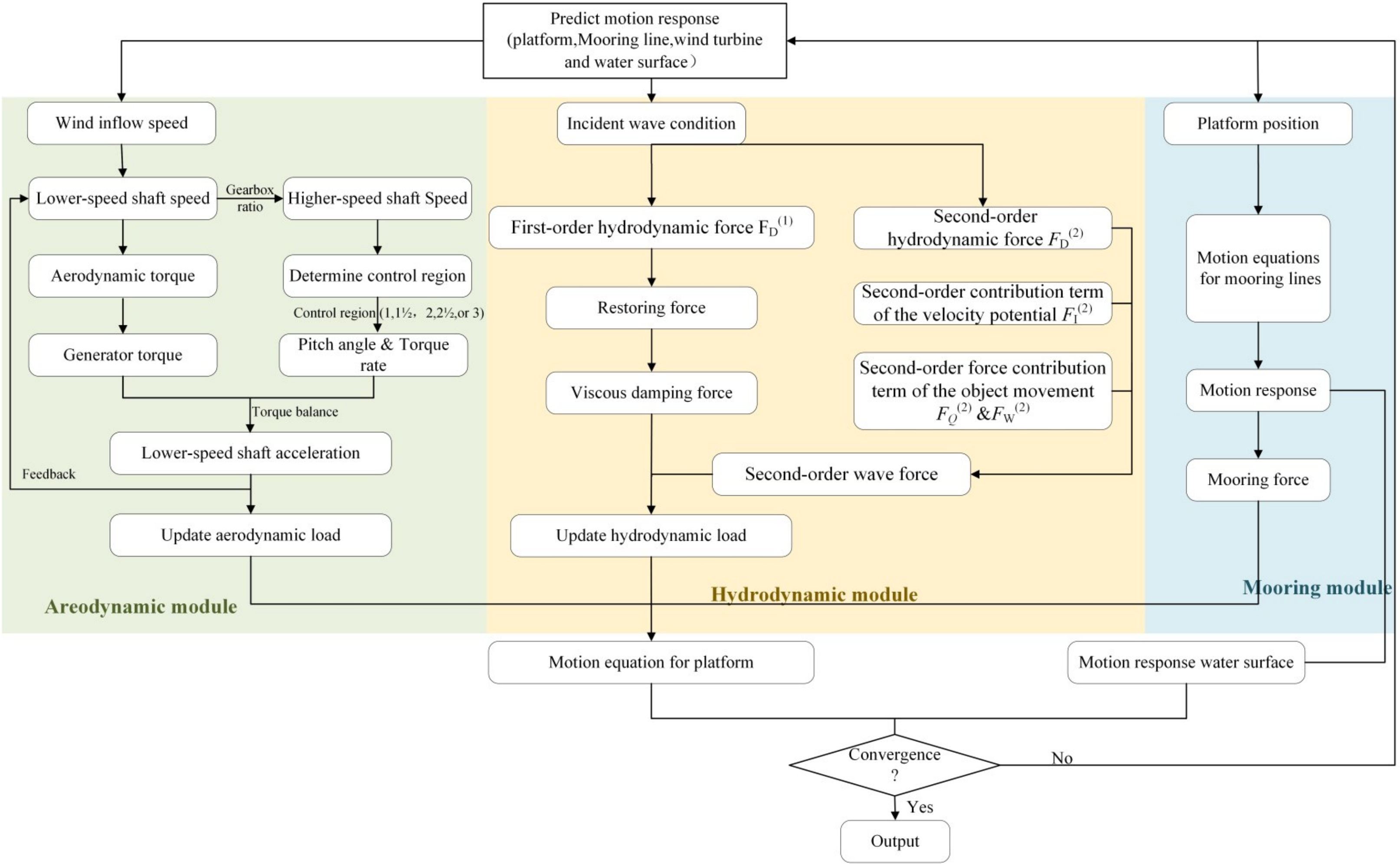

Fig. 4. Flow chart of the coupled dynamic analysis

3. Validation of the coupled numerical method

The NREL's 5-MW baseline wind turbine [45], supported by the OC4-DeepCwind semi-submersible platform, is chosen to demonstrate the accuracy and reliability of the developed method. The benchmark model in OpenFAST is specified in Robertson et al. [46]. The semi-submersible consists of one central column (CC 1) and three side columns (SC 1~3). Heave plates are attached at the bottom of the side columns to reduce the heave motion of the semi-submersible. Braces are used to connect the columns. The angle between two adjacent mooring lines is 120°. The wind and waves propagate in the direction parallel to the mooring line 2. Detailed properties are listed in Table 1. The experiment data are from the 1:50 scale model test conducted at Maritime Research Institute Netherlands (MARIN) in Wageningen, Netherlands [48, 49, 50].

This platform is used in the following simulation except in Subsection 3.1.2. The fully coupled model contains the hydrodynamic model, mooring system, and aerodynamic model. Individual verifications for each part are presented in Subsection 3.1-3.3.

Table 1. Main specifications of the OC4-DeepCwind semisubmersible FOWT [47]

Designation	Units	Value
Platform draft	m	20
Floater steel mass	kg	3.852×10^{6}
Total mass (Including WT)	kg	1.407×10^{6}
COG (x, y, z)	m, m, m	(0,0,-9.89)
Platform roll inertia about COG	$kg.m^2$	1.270×10^{10}
Platform pitch inertia about COG	$kg.m^2$	1.270×10^{10}
Platform yaw inertia about COG	$kg.m^2$	1.229×10^{10}

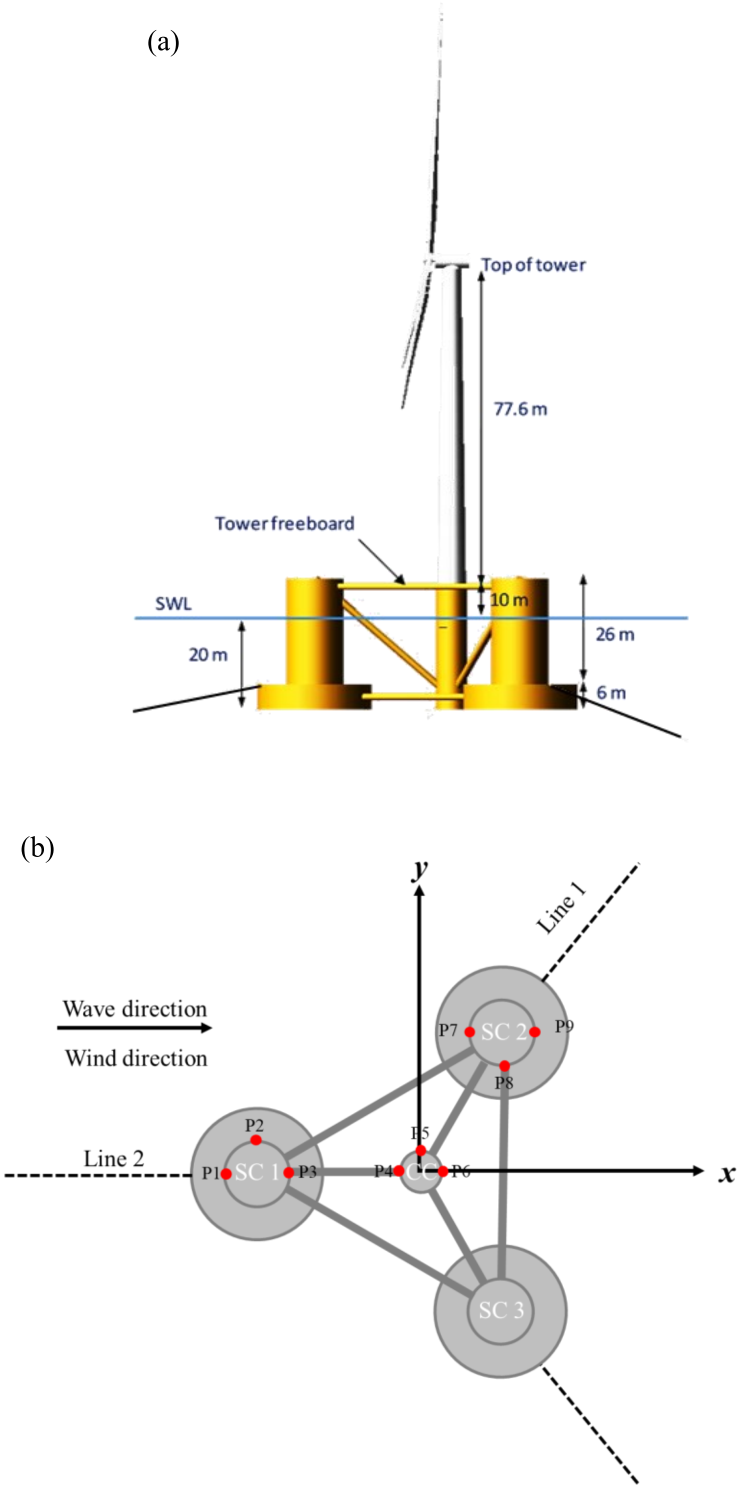

Fig. 6. DeepCwind floating wind turbine system (a) side view [47], (b) top view.

Spatial and temporal convergence tests of the platform are conducted. Using the symmetry property, there are 599 elements in the free surface grid and 307 elements in the object surface grid. The radius of the discretised free surface is 200m, with innermost elements size of 8.5m2 and outermost elements size of 1000m^2. The average number of elements on the main column and an offset column are 165 and 120, respectively. The time step is $T/100$, where T is the wave period. The specific schematic diagram of the grid is shown in Fig. 5.

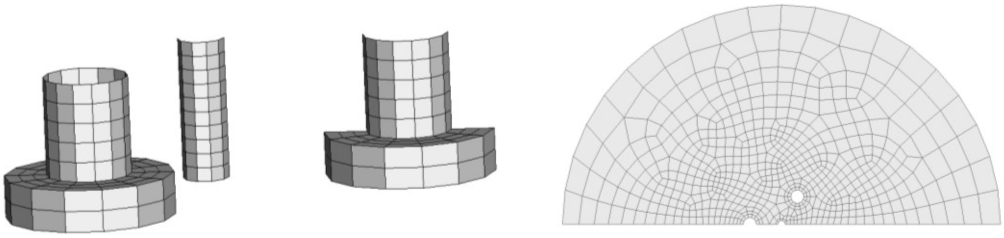

(a) (b)

Fig. 5. Schematic diagram of (a) the platform and (b) the free surface grid.

3.1 Validation of the hydrodynamic module

3.1.1 Free decay

Numerical validations on the hydrodynamics of the OC4 DeepCwind semisubmersible platform are performed before conducting comparative studies using fully coupled aero-hydrodynamic analysis on the entire configuration. The free decay response of the platform is considered first, thanks to the experimental data [50]. In the free decay analysis, the platform's initial position is set following the experimental conditions and then released to obtain free motions.

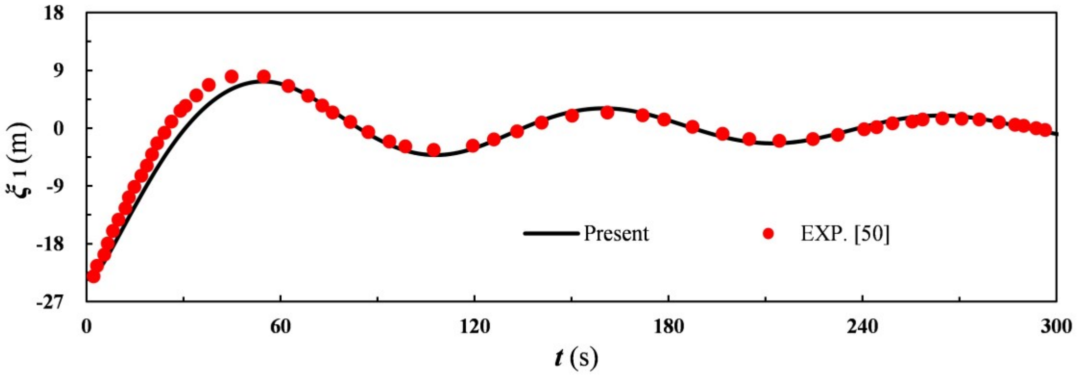

(a)

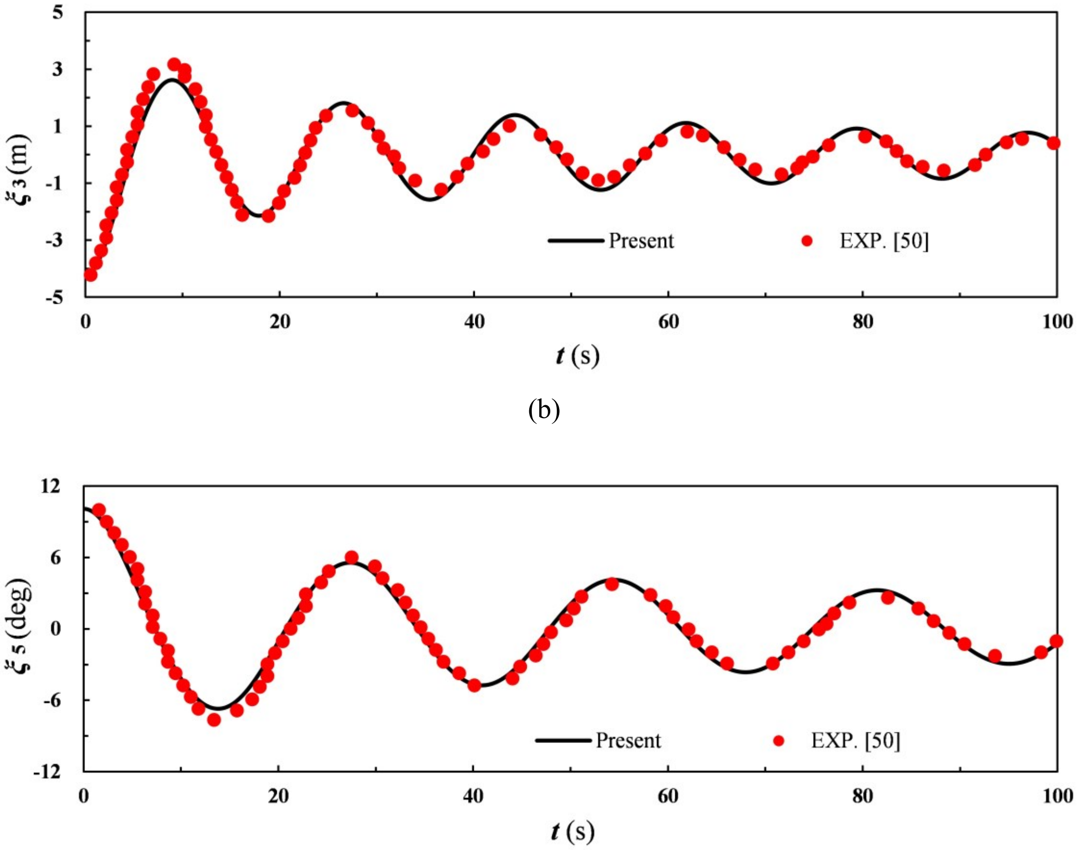

(b)

(c)

Fig. 7. Comparisons of free-decay responses in (a) surge, (b) heave, and (c) pitch.

There exist neither wind nor waves. It is assumed that the air damping can be neglected in the free decay analysis. In the test, the floating system is subjected to recovery forces provided by water and mooring cables, while the motions in all 6 DoFs are not restrained. Starting from the released position, the platform motion decays gradually until the mooring system reaches equilibrium. The results are compared with the experimental data [50], as shown in Fig. 7. In general, good agreements are found in the surge, heave and pitch motions.

Table 2. Comparison of the natural periods (unit: s)

DoF	Experiment [50]	Present
Surge	107	107
Sway	112	112
Heave	17.5	17.5

Roll	26.9	27
Pitch	26.8	26.8
Yaw	82.3	82

3.1.2 Nonlinear wave force on a vertical cylinder

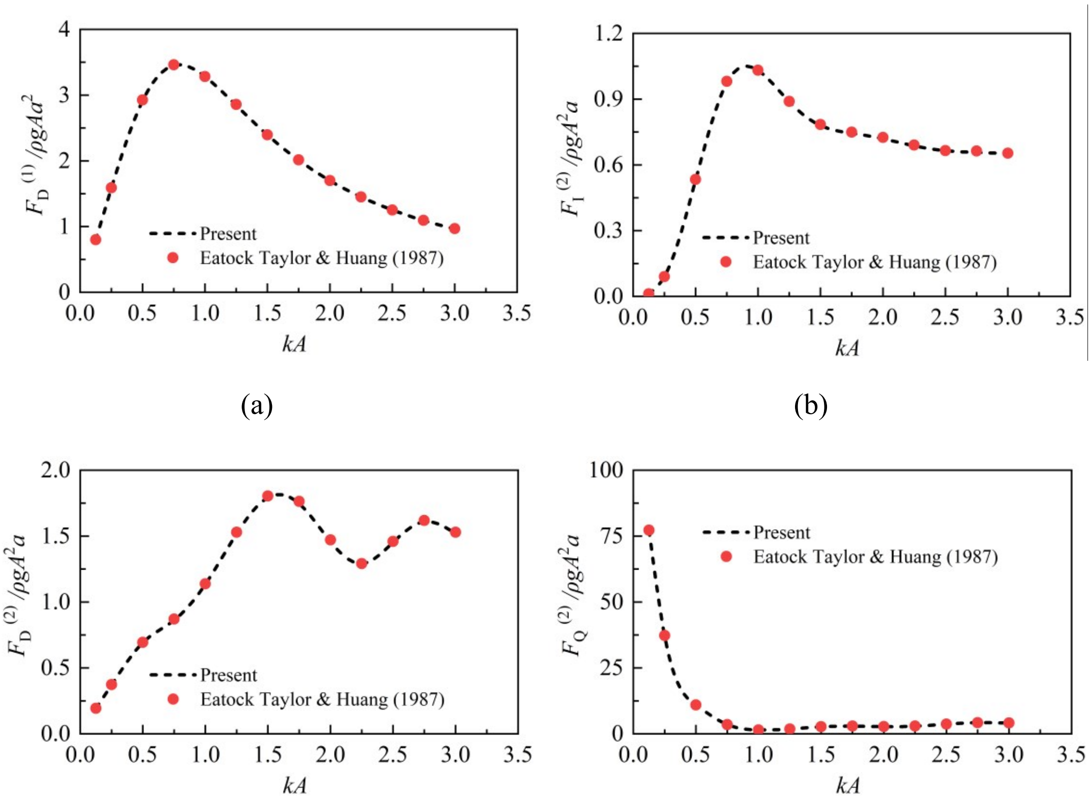

(a) (b)

(c) (d)

Fig. 8. Comparison of the wave force acting upon a bottom-fixed vertical cylinder: (a) the first-order amplitude, (b) mean drift force, (c) the sum-frequency amplitude contributed by the quadratic of first-order quantities, (d) the sum-frequency amplitude contributed by the second-order potential

A bottom-fixed vertical cylinder is selected to validate the second-order module. Incident regular waves consisting of first- and second-order components are considered. The numerical results are compared with the semi-analytical solution in Eatock Taylor and Huang [36]. The radius of the vertical cylinder is $a = 1.0$ m, the water depth $d = 1.0$ m, the regular wave amplitude $A = 1.0$ m, and the wave number $k = 0.125 \sim 3.0$ m^{-1}. An *xz*-plane symmetry is adopted in the calculation. Fig. 8 (a)-Fig. 8 (d) compare the first-order and the second-order wave forces in the horizontal direction. The force amplitudes are normalised by $\rho g A a^2$. The comparison shows a good agreement, justifying the accuracy of the nonlinear numerical model.

3.1.3 Wave force on OC4-DeepCwind semi-submersible FOWT

The semisubmersible is analysed in its undisplaced position under a finite water depth (200 m). The first- and second-order wave excitation loads are calculated using the direct time-domain simulation method described in Section 2.1. Results are presented in Fig. 9. For all these wave conditions, the first-order wave force in the positive *x*-direction agrees well with the results obtained from NREL using WAMIT [46]. Moreover, the second-order wave force obtained simultaneously can supplement the published data.

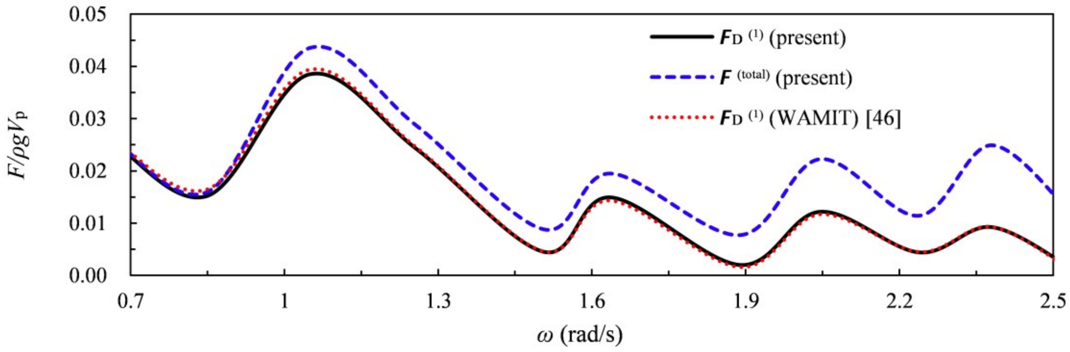

Fig. 9. Hydrodynamic wave excitation per unit amplitude on the OC4 semisubmersible

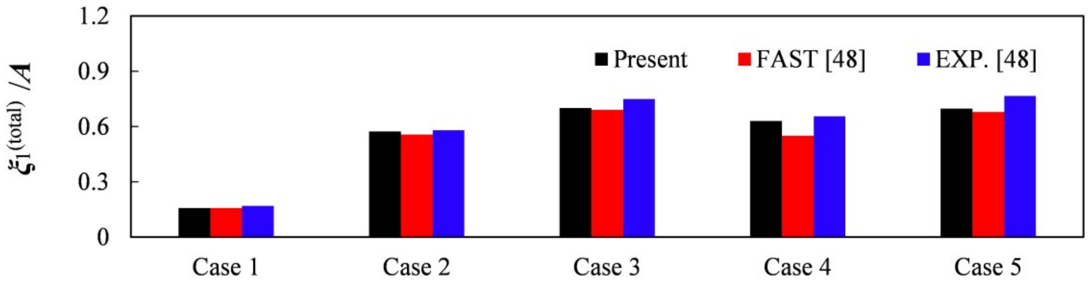

(a)

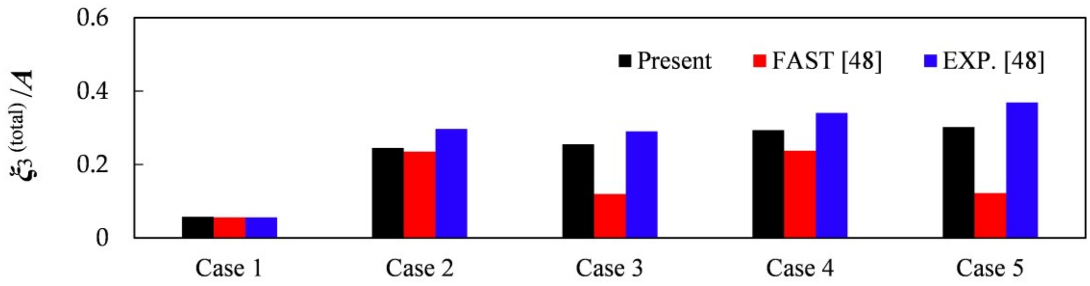

(b)

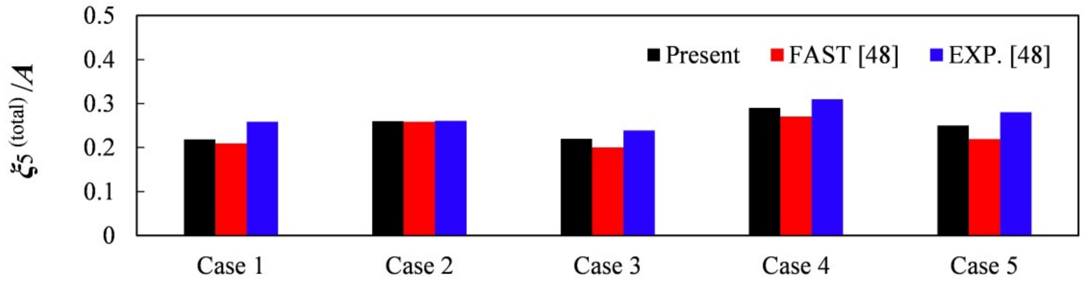

(c)

Fig. 10. Comparisons of RAOs of the platform: (a) surge RAO, (b) heave RAO, (c) pitch RAO

Table 2. Regular wave amplitudes and periods

	Case 1	Case 2	Case 3	Case 4	Case 5
A (m)	0.96	3.79	3.57	5.15	5.37
T (s)	7.5	12.1	14.3	12.1	14.3

In addition, the motion RAOs of the semisubmersible platform to regular waves in the absence of wind is investigated. Five different regular waves are considered based on Coulling et al. [48]. The amplitudes and periods are given in Table 2. All waves propagate in the positive x-direction.

The present results and the experiment results are nearly in accordance. It is noted that the heave response of the platform simulated in the current model is in better agreement with the experimental data in Fig. 10. The FAST simulation slightly underpredicts the heave response in almost all cases. The discrepancy is likely a result of the over-predict damping in the case of large amplitude heave scenarios [48].

3.2 *Mooring system*

The load-displacement relationship of an individual mooring line is given by the mooring system model. The quasi-static response of a separate mooring line as a function of the horizontal displacement from the fairlead to the anchor is shown in Fig. 11. In the OC4 design, the vertical distance between the fairlead and the anchor is fixed at 186 m. For detail, the readers are referred to Section 2.4 for the physical variables in Fig. 11. It is found that the differences between the results obtained from the present simulations and those calculated by NREL [46] are negligible.

-

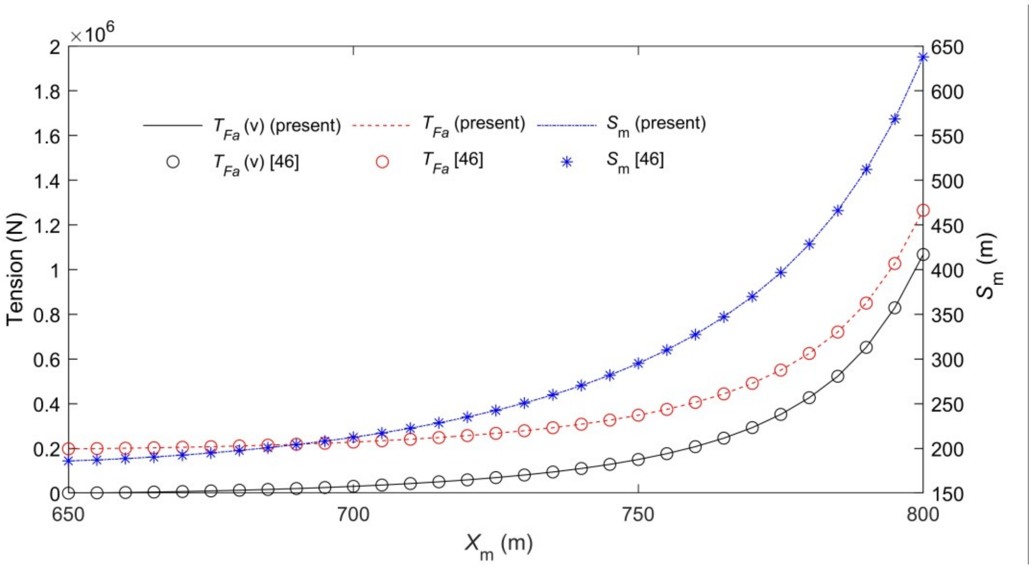

Fig. 11. Load-displacement relationships of a separate mooring line

3.3 *Wind turbine*

The simulations of the rotor are conducted at various uniform wind speeds from the cut-in (3m/s) to the rated wind speed (25m/s). The simulation results under each wind speed are recorded for enough long time to ensure that all initial transient behaviour has faded out. Fig. 12 displays the steady-state response of the 5-MW wind turbine. There are five control regions: 1, 1½, 2, 2½, and 3.

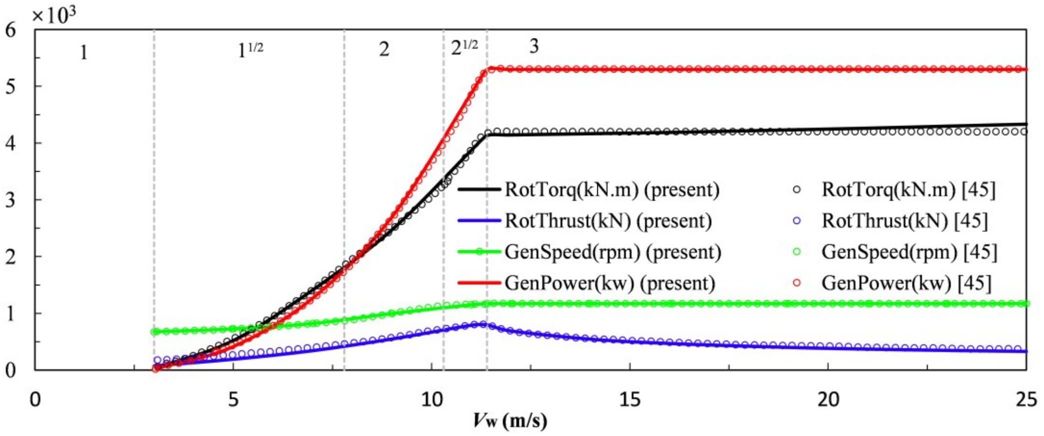

Fig. 12. Steady-state responses of the rotor

Region 1 is the control region before cutting in the wind speed, during which the generator torque is 0 and no power is obtained from the wind; in this process, the wind is used to accelerate the rotor before running the rotor. Region 1 ½ is a linear transition region between Region 1 and Region 2, applied to limit the lower operating generator speed. In Region 2, an optimum-mode variable-speed controller is used. Region 2 ½ is the linear transition between Region 2 and Region 3, and the torque slope equals the inducer slope. At rated power, Region 2 is usually required ½ to limit tip speed. The total pitch angle command of the full-span rotor blade is calculated in Region 3, and the speed error between the filtered generator speed and the rated generator speed is controlled by the gain preset proportional-integral (PI) [45]. For the above-rated wind speed conditions, variable blade-pitch configuration [43] takes over in Region 3. In this model, the blade pitch control system applied a simple single DoF model of the angular rotation of the shaft to adjust the generator speed and decrease the thrust on the turbine further. As shown in Figure 12, the characteristics of the rotor change a lot when the blade pitch control method is adopted. Meanwhile, the current results are almost consistent with the NREL study [46].

3.4 Fully coupled aero-hydrodynamic simulation

The fully coupled model is validated by the published numerical data [33] through the case study of a 5 MW wind turbine supported by the DeepCwind semisubmersible platform. The fully coupled aero-hydrodynamic simulation for the full-scale DeepCWind OC4 model is conducted under steady wind and regular wave conditions. In this case, the wind speed (*V*), the wave amplitude (*A*), and the wave period (*T*) are assumed to be 11 m/s, 3.79 m, and 12.1 s, respectively. Because the published CFD data is conducted without PI control, PI control is also not adopted in this simulation. Besides, some assumptions are made in all of the subsequent computations to perform consistent and objective validations: (1) the ignored effect on structural deformation, (2) the constant rotating speed of the blade and the blade pitch angle, and (3) quadratic viscous damping for simplifying the calculation of slender members.

Fig.13 compares the rotor thrust force and the aerodynamic power. It is found that no matter which method is used, the rotor thrust force varies from 780 kN to 950 kN with an average value of 865 kN. The aerodynamic power ranges from 5.5 MW to 3.5 MW, with an average value of 4.5 MW. Note that the phases are quite different due to the variation of the view wind speed changed by the platform motion, as explained in Fig.15.

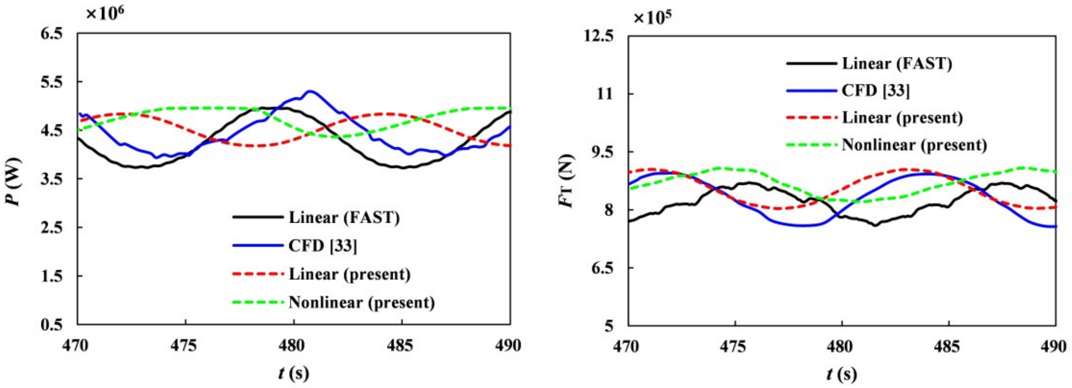

(a) (b)

Fig.13. Validation of the aerodynamic module: (a) rotor thrust and (b) aerodynamic power

Fig. 14 compares the mooring line tensions of Line 1 (at lee side) and Line 2 (at weather side). The average values of the CFD results are higher than the others, probably because the CFD results use a different initial mooring tension. It is found that the tension of Line 2 attached to the weather side of the platform is more likely to be influenced than Line 1 attached to the lee side. Besides, involving the second-order wave loads slightly increases the average value of the lee-side line but reduces that of the weather-side line.

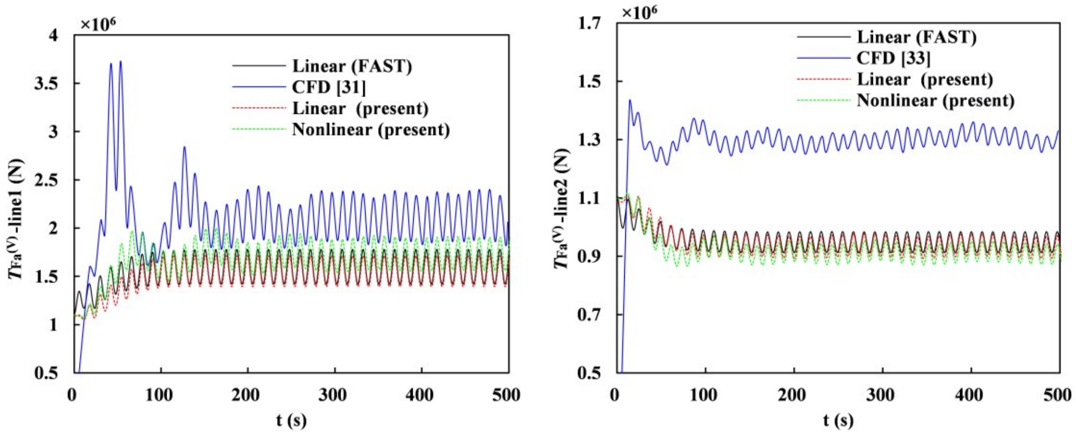

(a) (b)

Fig.14. Validation of the mooring system module: the line tensions in (a) Line 1, (b) Line 2.

Fig.15 validates the platform motion responses in a combined wind and wave condition. Due to the symmetry of the platform and the external loads, the responses in sway, roll, and yaw are not shown here since they are negligible. In general, the results from all the methods have similar trends in the three primary DoFs. Nevertheless, there are some noticeable differences. In surge, as given in Fig.15(a), although the motion amplitudes (ranging from 2.06 m to 2.21 m, see Table 3) and the phases ($T/12$) are almost the same, the mean positions of the platform calculated by the CFD method [33] and the nonlinear time-domain method are further away from those calculated by FAST (linear and nonlinear) or the present linear time-domain method. Besides, the nonlinear results [33] calculated by FAST and the nonlinear results in the present model differ greatly, which indicates that using the QTF based on the zero response assumption in the indirect time-domain method is not accurate enough for a moving floating structure. A direct time-domain method is necessary to model a moving floating wind turbine in nonlinear wave conditions. In heave, as given in Fig.15(b), the mean displacements and the phases of the platform are nearly identical except for the motion amplitude. The motion amplitude calculated by the CFD method is smaller than the others because it considers viscous damping more rigorously, while the others use empirical values. In pitch, as given in Fig.15(c), the mean displacements and the motion amplitudes are similar. However, there are small shifts in the phases due to the accumulation of slight phase differences from the initial moment. A buffering function is employed in the present method to suppress the large instantaneous motion at the initial moment.

Table. 3. Statistics of the steady-state platform surge response (unit: m)

Method	Max	Min	Mean	Amplitude
Linear (FAST)	10.2474	5.8895	8.0684	2.1789
Linear (present)	10.2700	5.8970	8.0835	2.1865
CFD [33]	11.3842	7.2632	9.3237	2.0605
Nonlinear (present)	11.9050	7.4786	9.6918	2.2132
Nonlinear (FAST) [33]	10.2560	5.7473	8.00165	2.25135

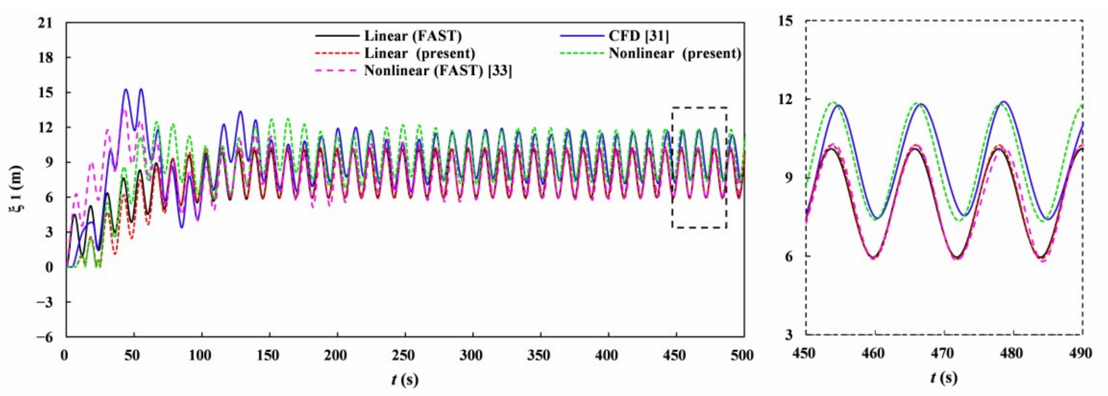

(a)

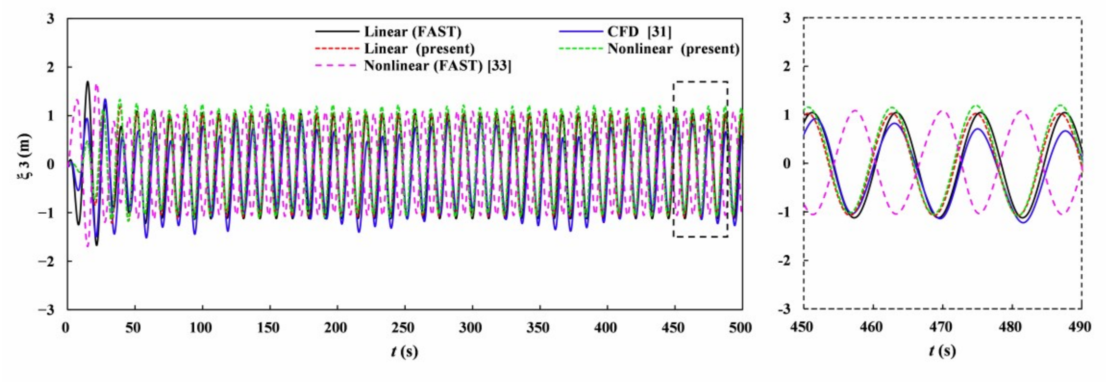

(b)

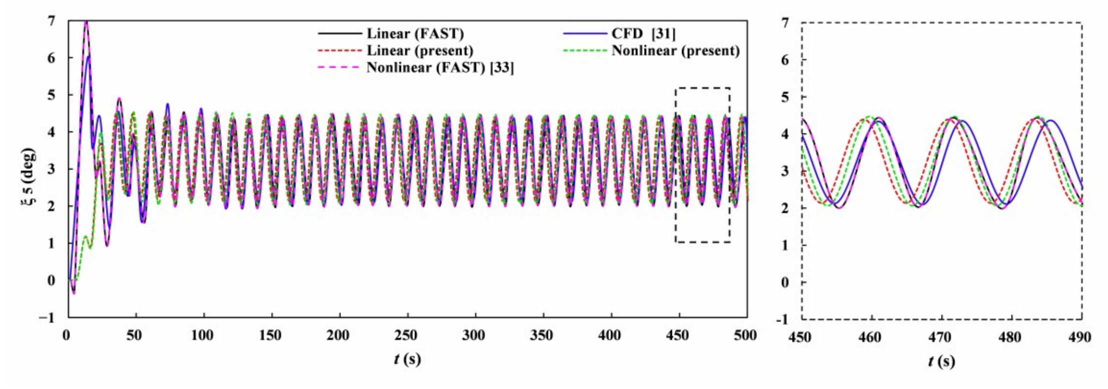

(c)

Fig.15. Validation of the coupled dynamic module: the platform motion responses in (a) surge, (b) heave, and (c) pitch

4. Coupled and nonlinear effects on FOWT

To investigate the coupled nonlinear effects on FOWT, three cases are compared under the action of linear or nonlinear wave force in this section, (1) a 5 MW NREL baseline wind turbine atop a moored OC4 DeepCwind semisubmersible platform, (2) a moored bare DeepCwind platform, and (3) a freely-floating bare DeepCwind platform. These cases hereafter are referred to as LC1, LC2, and LC3, respectively.

Table. 4. Configuration for each case

Load case	Wind condition	Wave condition	Mooring system condition
LC1	uniform wind V= 11 m/s	regular wave A= 3.79 m; T= 12.1 s	three mooring lines
LC2	without wind	regular wave A= 3.79 m; T= 12.1 s	three mooring lines
LC3	without wind	regular wave A= 3.79 m; T= 12.1 s	freely-floating, no mooring

Fig.16 depicts the platform motion responses to different load conditions. It is found that the mean displacements of surge and pitch motions in LC1 are significantly larger than LC2 and LC3 due to the additional aerodynamic thrust on the wind turbine. In contrast, the heave motion is not affected by the aerodynamic thrust. It is found that, under the action of the non-linear wave force up to the second-order, the platform surge response can be decomposed into two parts, i.e., a wave-frequency sinusoidal motion and a low-frequency motion. The wave-frequency motion has the same period as the linear incident wave, indicating that it is mainly caused by the linear wave force. Besides, compared to Figure 16(a), Figure 16(b) exhibits a slow drift motion whose period is close to the platform's surge natural period as given in Table 2, implying that the existence of the second-order wave force excites the low-frequency motion. Without the restraining from the mooring system, the platform gradually drifts away in LC3 due to the wave drift loads in Fig.16(b). In the presence of mooring, although the amplitude of the linear motion at the wave frequency does not change, the amplitude of the slow drift motion decreases with time in LC1 and LC2. Moreover, the amplitude and the phase of the slow drift motion are less in LC1 than in LC2 since the drift displacement of the platform induced by the wind force in LC1 further increases the mooring stiffness [46].

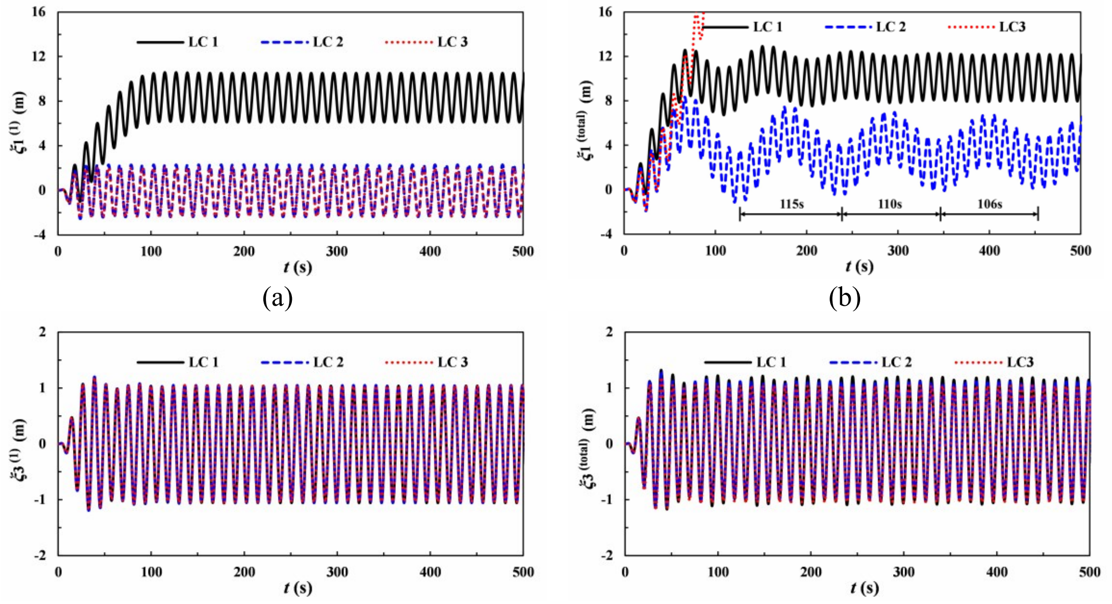

(a) (b)

(c) (d)

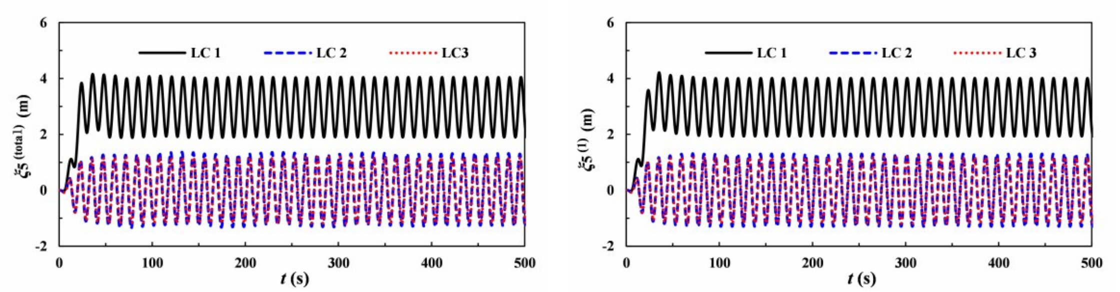

(e) (f)

Fig.16. Platform motion responses to different load conditions: (a) surge response to linear wave force, (b) surge response to nonlinear wave force, (c) heave response to linear wave force, (d) heave response to nonlinear wave force, (e) pitch response to linear wave force, and (f) pitch response to nonlinear wave force.

Fig. 17 shows the linear and nonlinear wave forces on the platform. The linear components are generally the same in all cases. However, there is a significant discrepancy considering the nonlinearity. The total wave force along the *x*-axis, $F_1^{(total)}$, exhibits an apparent secondary load cycle [53] in LC1, and the maximum wave force in LC1 is less than LC2 and LC3. The total wave moment with respect to the *y*-axis, $F_5^{(total)}$, which also exhibits a secondary load cycle in LC1, has a larger peak value in LC1 than in the other two cases. The reason is that the aerodynamic thrust in LC1 enlarges the platform pitch motion and, associatively, the surge motion, which significantly alters the wave force on the platform. Moreover, the results indicate that the coupled motion does not influence the linear wave force much, but rather the nonlinear wave force.

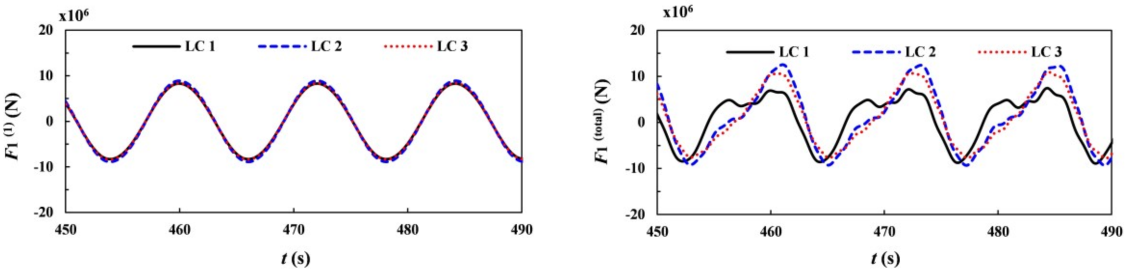

(a) (b)

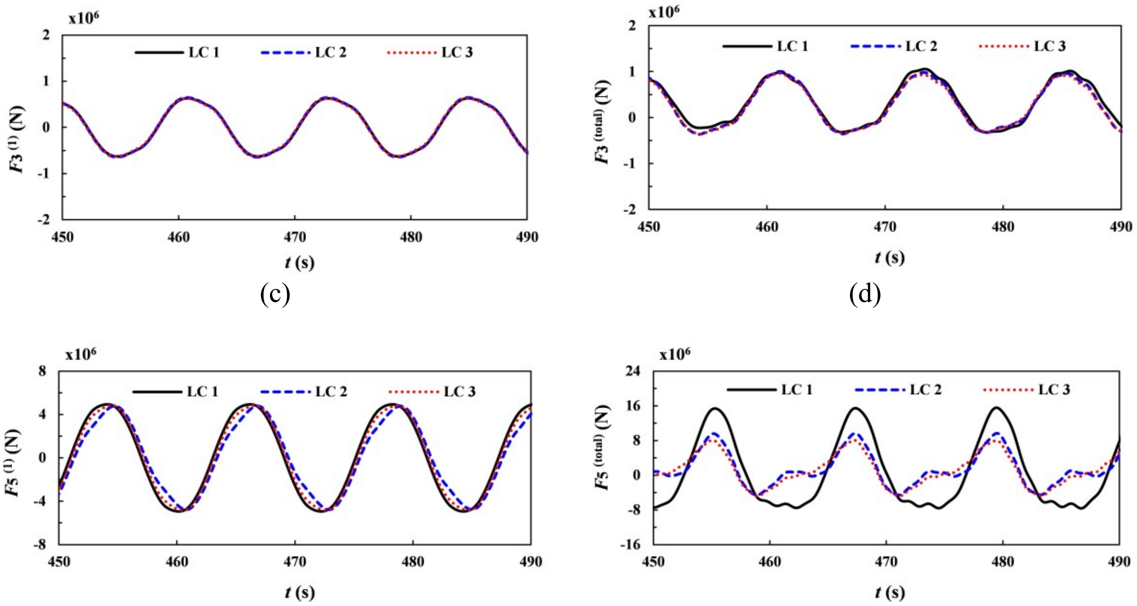

(c) (d)

(e) (f)

Fig.17. Comparison of (a) linear wave force along the *x*-axis, (b) nonlinear wave force along the *x*-axis, (c) linear wave force along the *z*-axis, (d) nonlinear wave force along the *z*-axis, (e) linear wave moment with respect to the *y*-axis, and (f) nonlinear wave moment with respect to the *y*-axis

As explained in Eq. (11), wave forces upon a floating structure are directly influenced by the wave runups. A further comparison is thus made on the surrounding wave elevation. Fig.18 provides instantaneous plots of waves passing through the platform, where the platform is set to be motion-fixed in LC3. The time increment between successive images is $\Delta t = 2$ s. A group of 4 plots in each case corresponds to approximately a time period of $T/2$. The incident waves propagate rightwards from the left side of each plot. With the arrival of a wave crest, the water is driven up to the weather-side surface of the left column. A notable parenthesis-shaped water mound occurs in the middle of the platform immediately following the passage of the wave crest. Then, the waves propagate in the downstream direction, and the wave trough creates a similar effect on the lee-side surface of the columns.

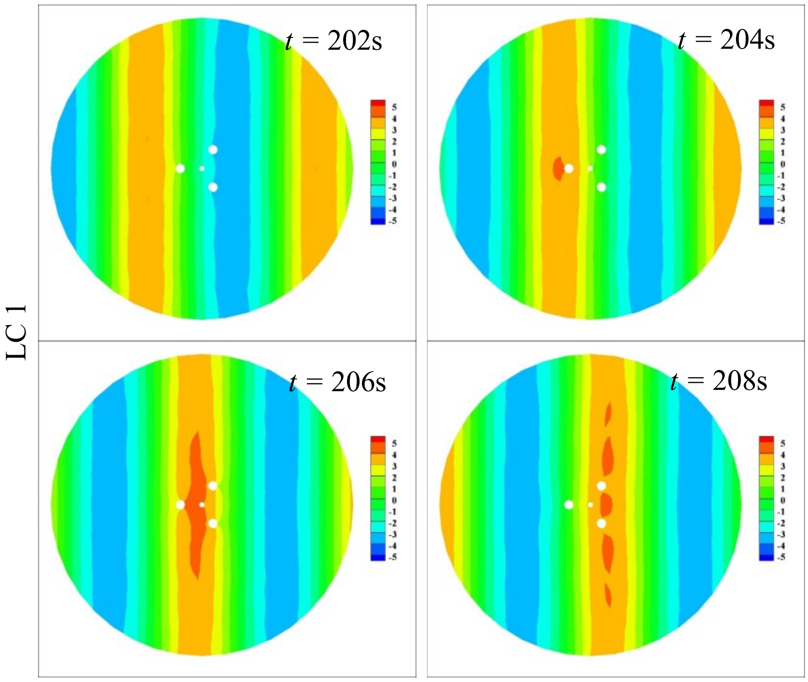

LC 1
t = 202s
t = 204s
t = 206s
t = 208s
5
4
3
2
1
0
-1
-2
-3
-4
-5

(a)

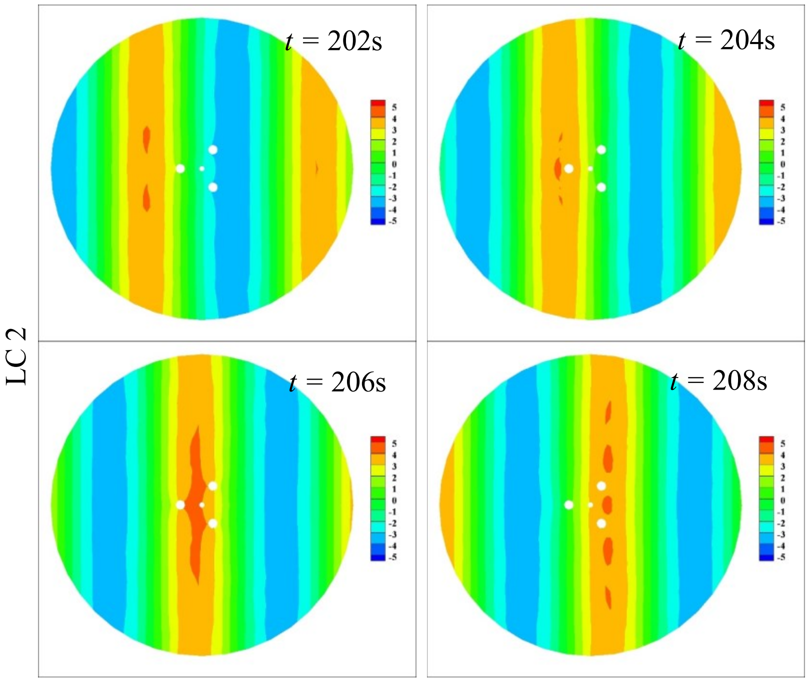

LC 2
t = 202s
t = 204s
t = 206s
t = 208s
5
4
3
2
1
0
-1
-2
-3
-4
-5

（b）

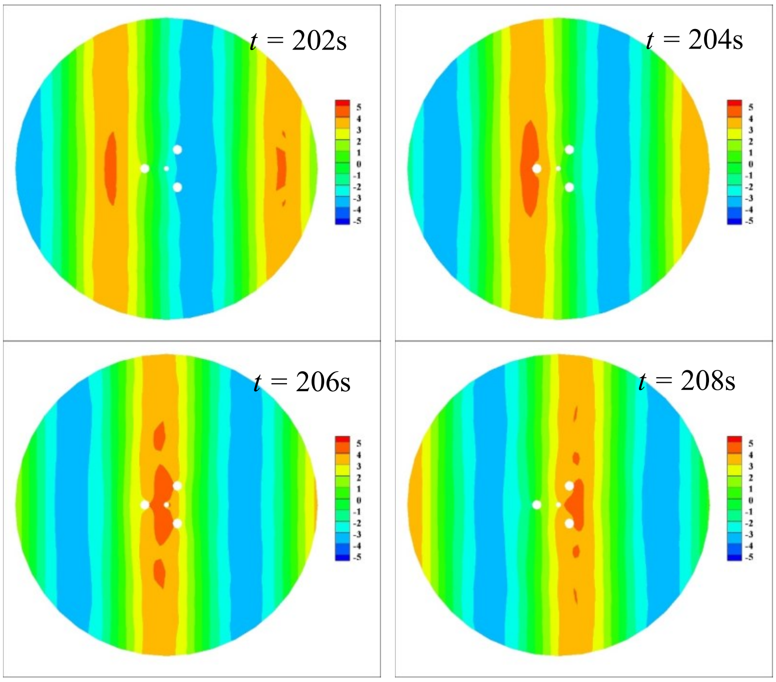

(c)

Fig.18. Wave elevation in (a) LC 1, (b) LC 2, (c) LC 3 (fixed).

Wave elevations at some critical locations around the platform, P_i, are further plotted in Fig. 19. The spatial coordinates of P_i are listed in Table 5. P1~3, P4~6 and P7~9 are set around the left-hand side column SC1, the central column CC1, and the upper right-hand side column SC2 (see Fig.6 for the layout), respectively. When the wave passes through SC1 and CC1, the maximum wave elevation exists on the shoulder of the column (P2 & P5) in LC1 and on the weather side of the column (P1 & P4) in LC2 and LC3. On the contrary, when the wave passes through SC2, the maximum wave elevation exists on the shoulder of SC2 (P8) in LC1 and on the lee side of SC1 (P9) in LC2 and LC3. To explain the fluid mechanism clearly, the platform is set to be motion-fixed in LC3. It is found that the wave elevations are all different in the three load cases, which means that the wave elevation depends on the motion of the platform. Therefore, there is a strong interaction effect between the wave field and the structure motion. The structure motion may change the wave field in real time, which can not be taken into account in the indirect time-domain method. For this reason, a direct time-domain method is necessary for understanding the motion response of a fully coupled FOWT in nonlinear waves.

Table. 5. The coordinates of the points

Axis	P1	P2	P3	P4	P5	P6	P7	P8	P9
x	-34.87	-28.87	-22.87	-3.25	0.00	3.25	20.44	14.44	8.44
y	0.00	5.85	0.00	0.00	3.25	0.00	25.00	19.00	25.00

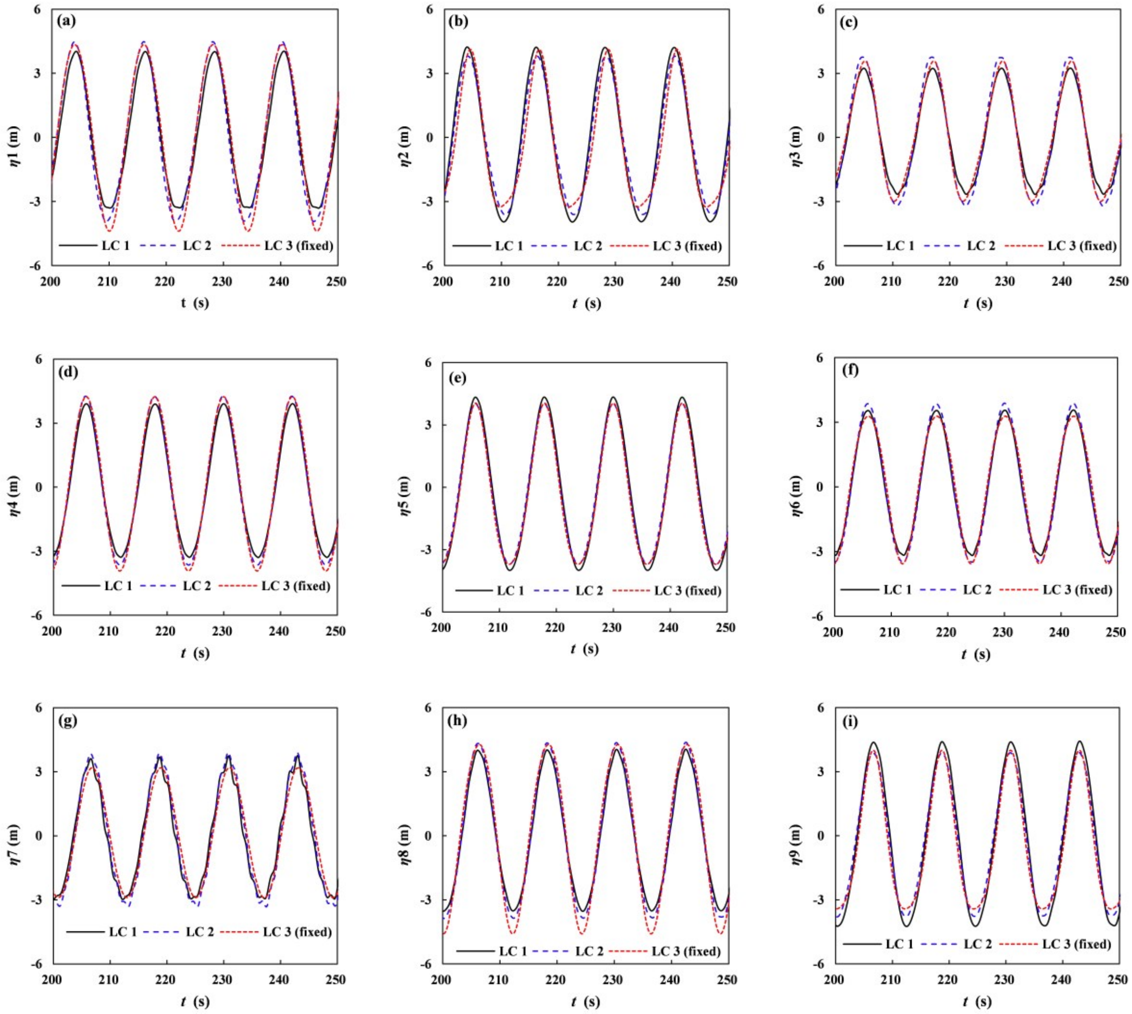

Fig.19. Wave elevation at some points around the platform surface: (a) P1, (b) P2, (c) P3, (d) P4, (e) P5, (f) P6, (g) P7, (h) P8, and (i) P9

5. Conclusion

In this study, a direct time-domain method is proposed to calculate the wave force acting on the floating foundation of a floating wind turbine in nonlinear waves. In the numerical method, the body surface and the free water surface are discretised by quadratic elements. The direct time-domain method is then incorporated with the blade element method and the catenary theory to model a full FOWT configuration consisting of a wind turbine atop a floating platform restrained by mooring lines. Each part of the coupled model is validated against experimental or numerical results published in the literature. These validations include (1) linear and nonlinear wave excitation loads, (2) free-decay motion, (3) load-displacement relationship, and (4) steady-state responses of the wind turbine rotor. After that, validation is conducted on the fully coupled aerodynamic-hydrodynamic model against FAST and CFD, justifying the accuracy and effectiveness of the present method. These results illustrate that the traditional indirect time-domain method using the QTF based on the zero-response assumption cannot appropriately evaluate the nonlinear wave force on a FOWT in coupled motions.

Furthermore, the coupled nonlinear effect on the OC4 DeepCwind semisubmersible FOWT in the combined wind and wave conditions is investigated. It is found that the nonlinear wave force mainly influences the surge motion, leading to a wave-frequency sinusoidal motion driven by the linear wave force and a low-frequency slow drift motion driven by the wave drift loads. Further analysis of the wave field and the maximum wave elevation distribution around the platform shows that the FOWT motion is vital. For this reason, a direct time-domain method is necessary for understanding the motion response of a fully coupled FOWT in nonlinear waves.

Acknowledgement

The corresponding author greatly thanks the financial support from National Natural Science Foundation of China (Grant No. U22A20242) and Liaoning Revitalization Talents Program (Grant No. XLYC2002033)

Reference

---

[1] International Energy Agency, Offshore Wind Outlook 2021. World Energy Outlook Special Report, (2022).

[2] BK. Bose, Global Warming: Energy, Environmental Pollution, and the Impact of Power Electronics, IEEE Industrial Electronics Magazine, (2010) 4(1): 6-17.

[3] S.P. Breton, G. Moe, Status, plans and technologies for offshore wind turbines in Europe and North America, Renewable Energy, (2009) 34(3): 646-654.

[4] M.S. Gen, F. Karipoğlu, K. Koca, ŞT. Azgın, Suitable site selection for offshore wind farms in Turkey's seas: GIS-MCDM based approach, Earth Science Informatics, (2021) 14(3):1213–25.

[5] L. Eatough, Floating offshore wind technology and operations review, Offshore Renewable Energy Catapult, (2021).

[6] The global wind atlas, (2020).

[7] N. Luo, J.L.P. Garcés, Y.V. Seguí, M. Zapateiro, Dynamic load mitigation for floating offshore wind turbines supported by structures with mooring lines, àrees temàtiques de la upc::energies::energia eòlica, (2012).

[8] P. Cheng, Y. Huang, D. Wan, A numerical model for fully coupled aero-hydrodynamic analysis of floating offshore wind turbine, Ocean Engineering, (2019) 173(FEB.1):183-196.

[9] J.M. Jonkman, M.L. Buhl, FAST user's guide, (2005).

[10] T.V. Zandt, FAST User's Guide, (2007).

[11] J.M. Jonkman, A.N. Robertson, G.J. Hayman, HydroDyn user's guide and theory manual, National Renewable Energy Laboratory, (2014).

[12] Y. Yang, M. Bashir, C. Michailides ,C. Li, J. Wang, Development and application of an aero-hydro-servo-elastic coupling framework for analysis of floating offshore wind turbines, Renewable Energy, (2020).

[13] D. Roddier, C. Cermelli, A. Aubault, WindFloat: A Floating Founda-Tion for Offshore Wind Turbines Part II Hydrodynamics Analysis, (2009).

---

[14] M.I. Kvittem, E.E. Bachynski, T. Moan, Effects of hydrodynamic modeling in fully-coupled simulations of a semisubmersible wind turbine, Energy Procedia, (2012)24: 351-362.

[15] S. Shim, Coupled Dynamic Analysis of Floating Offshore Wind Farms, Doctoral dissertation, Texas A & M University, (2010).

[16] M. Karimirad, Modeling aspects of a floating wind turbine for coupled wave–wind-induced dynamic analyses, Renewable Energy, (2013)53(MAY):299-305.

[17] MARINTEK. Simo theory manual. Trondheim, Norway: Sintef, (2009).

[18] MARINTEK. Riflex theory manual. Trondheim, Norway: Sintef, (2008).

[19] T.J. Larsen, A.M. Hansen. HAWC2 user manual. Denmark: Risø National Laboratory, Technical University of Denmark, (2008).

[20] C. L. Cunff, J.M. Heurtier, L. Piriou, C. Berhault, T. Perdrizet, D. Teixeira, J.C. Gilloteaux, Fully-coupled floating wind turbine simulator based on nonlinear finite element method: Part Id-methodology, in: ASME 2013 32nd International Conference on Ocean, Offshore and Arctic Engineering, American Society of Mechanical Engineers Digital Collection, (2013).

[21] T. Perdrizet, J.C. Gilloteaux, D. Teixeira, G. Ferrer, L. Piriou, D. Cadiou, C. L. Cunff, Fully-coupled floating wind turbine simulator based on nonlinear finite element method: Part IIdvalidation results, in: ASME 2013 32nd International Conference on Ocean, Offshore and Arctic Engineering, American Society of Mechanical Engineers Digital Collection, (2013).

[22] Y. Liu, C. Hu, M. Sueyoshi, S. Yoshida, H. Iwashita, M. Kashiwagi. Motion response characteristics of a Kyushu-University semisubmersible floating wind turbine with trussed slender structures: experiment vs numerical simulation. Ocean Engineering (2021) 232, 109078.

[23] Y. Liu, C. Hu, S. Yoshida. Time-domain response of a semisubmersible floating wind turbine with trussed slender structures. In: Proc. of the 14th ISOPE Pacific-Asia Offshore Mechanics Symposium, Dalian, China, Nov. 22–25, 2020.

[24] J. Chen, Z. Hu, G. Liu, D. Wan, Coupled aero-hydro-servo-elastic methods for floating wind

turbines, Renewable Energy, (2019)130:139-153.

[25] F. Lemmer, W. Yu, P.W. Cheng, Iterative Frequency-Domain Response of Floating Offshore Wind Turbines with Parametric Drag. Journal of Marine Science and Engineering, (2018)6(4):118.

[26] F. Gordon, M. David, M. Emil, Design of a semisubmersible platform for a 5MW wind turbine, in: 44th AIAA Aerospace Sciences Meeting and Exhibit, (2006): 997.

[27] A. Beardsell, A. Alexandre, B. Child, R. Harries, D. McCowen, Beyond OC5eFurther advances in floating wind turbine modelling using Bladed, Journal of Physics: Conference Series, (2018):1102, 012023-.

[28] F. G. Nielsen, T. D. Hanson, B. Skaare, Integrated Dynamic Analysis of Floating Offshore Wind Turbines, 25th International Conference on Offshore Mechanics and Arctic Engineering, (2006).

[29] B. Skaare, TD. Hanson, F. G. Nielsen, Importance of Control Strategies on Fatigue Life of Floating Wind Turbines. Asme International Conference on Offshore Mechanics & Arctic Engineering, (2007).

[30] A.E. Loken, Three Dimensional Second Order hydrodynamic Effects on Ocean Structures in Waves. Rep. UR-86-54. University of Tronheim, Dept of Marine Technology, (1986).

[31] P.W Cong, Y. Gou, B. Teng , A new approach to low-frequency QTF and its application in predicting slow drift force, Ocean Engineering, 53, 25–37,(2012).

[32] B. Teng, P. W. Cong, Y. Gou, Examination on low-frequency qtf of a platform. Journal of Hydrodynamics, (2010)Ser.B, 22(5-supp-S1): 969-974.

[33] T. T. Tran, D. H. Kim, Fully coupled aero-hydrodynamic analysis of a semisubmersible fowt using a dynamic fluid body interaction approach, Renewable Energy, (2016).

[34] C.K. Wu, V. Nguyen, Aerodynamic simulations of offshore floating wind turbine in platform-induced pitching motion, Wind Energy, (2017)20 (5):835–858.

[35] Y. C. Liu, Q. Xiao, A. Incecik, C. Peyrard, D. Wan,Establishing a fully coupled CFD analysis tool for floating offshore wind turbines, Renewable Energy, (2017)112:280-301

[36] R. E. Taylor, S. M. Hung, Second order diffraction forces on a vertical cylinder in regular waves, Applied Ocean Research, (1987)9(1):19-30.

[37] P. Ferrant, Three dimensional unsteady wave-body interactions by a rankine boundary element method. Ship Technology Research, (1993)40:165–175

[38] W. Bai, B. Teng, Simulation of second-order wave interaction with fixed and floating structures in time domain, Ocean Engineering, (2013)74:168–177.

[39] R. Jin, B. Teng, D. Ning, M. Zhao, L. Cheng, Numerical investigation of influence of wave directionality on the water resonance at a narrow gap between two rectangular barges, Acta Oceanologica Sinica, (2017)36:104–111.

[40] P. J. Moriarty, A. C. Hansen, Aerodyn theory manual, National Renewable Energy Laboratory, (2005).

[41] M. Hansen, Aerodynamics of wind turbines, Routledge, (2015).

[42] H. Glauert, Airplane propellers, Aerodynamic Theory, (1935).

[43] L. U. Dan-Hong, L. I. Qing, , Y. F. Zhang, X. Y. Zhang, Simulation of variable blade pitch wind turbine. Techniques of Automation and Applications, (2011).

[44] A. Jain, Dynamic behavior of offshore spar platforms under regular sea waves, Ocean Engineering, (2003)30(4): 487-516.

[45] J. M. Jonkman, S. Butterfield, W. Musial, G. Scott, Definition of a 5mw reference wind turbine for offshore system development, Office of Scientific & Technical Information Technical Reports, (2009).

[46] A. Robertson, J. Jonkman, M. Masciola, H. Song, A. Goupee, A. Coulling, C. Luna, Definition of the semisubmersible floating system for phase II of OC4, Scitech Connect Definition of the Floating System for Phase IV of Oc3, (2014).

[47] L. Zhang, W. Shi, M. Karimirad, C. Michailides, Z. Jiang, Second-order hydrodynamic effects on the response of three semisubmersible floating offshore wind turbines, Ocean engineering,

(2020):207.

[48] A. J. Coulling, A. J. Goupee, A. N. Robertson, J. M. Jonkman, H. J. Dagher, Validation of a FAST semisubmersible floating wind turbine numerical model with DeepCwind test data, Journal of Renewable & Sustainable Energy, (2013)5(2):557-569.

[49] Dagher, Habib, Viselli, Anthony, Goupee, Andrew, and Allen, Christopher, 1:50 Scale Testing of Three Floating Wind Turbines at MARIN and Numerical Model Validation Against Test Data. United States , (2017).

[50] S. Gueydon, S. Welle, Study of a floating foundation for wind turbines. Journal of Offshore Mechanics and Arctic Engineering, (2013):135(3).

[51] J. M. Jonkman, A. N. Robertson, G. J. Hayman, HydroDyn user's guide and theory manual, National Renewable Energy Laboratory, (2014).

[52] M.O.L. Hansen, Aerodynamics of Wind Turbines, Science Publishers, James and James (Science Publishers) Ltd, (2000).

[53] J. Grue, G. Bjorshol, O. Strand, Nonlinear wave loads which may generate 'ringing' responses of offshore structures. In Proceedings of International Workshop on Water Waves and Floating Bodies, Japan, (1994).